PAPER

Check for updates

Comprehensive analysis of crystal structure, spectroscopic properties, quantum chemical insights, and molecular docking studies of two pyrazolopyridine compounds: potential anticancer agents†

Efraín Polo-Cuadrado, [ID] [a] Lorena López-Cuellar,[ab] Karen Acosta-Quiroga,[c] Cristian Rojas-Peña,[c] Iván Brito, [ID] [d] Jonathan Cisterna,[e] Jorge Trilleras, [ID] [f] Joel B. Alderete,[g] Yorley Duarte*[hi] and Margarita Gutiérrez [ID] *[a]

In this study, two pyrazolo[3,4-*b*]pyridine derivatives (**4a** and **4b**) were grown using a slow evaporation solution growth technique and characterized by FT-IR, HRMS, ^{1}H/^{13}C NMR spectroscopy, and X-ray crystallography. The **4a** and **4b** structures crystallized in monoclinic and triclinic systems with space groups $P2_1/n$ and $P\bar{1}$, respectively. Theoretical calculations were performed at the DFT/B3LYP level for the optimized geometries. The results were in excellent agreement with the experimental data (spectroscopic and XRD). This investigation encompasses molecular modeling studies including Hirshfeld surface analysis, energy framework calculations, and frontier molecular orbital analysis. Intermolecular interactions within the crystal structures of the compounds were explored through Hirshfeld surface analysis, which revealed the notable presence of hydrogen bonding and hydrophobic interactions. This insight provides valuable information on the structural stability and potential solubility characteristics of these compounds. The research was extended to docking analysis with eight distinct kinases (BRAF, HER2, CSF1R, MEK2, PDGFRA, JAK, AKT1, and AKT2). The results of this analysis demonstrate that both **4a** and **4b** interact effectively with the kinase-binding sites through a combination of hydrophobic interactions and hydrogen bonding. Compound **4a** had the best affinity for proteins; this is related to the fact that the compound is not rigid and has a small size, allowing it to sit well at any binding site. This study contributes to the advancement of kinase inhibitor research and offers potential avenues for the development of new therapeutic agents for cancer treatment.

1. Introduction

Kinases are naturally occurring enzymes that play an important role in the regulation of cellular and physiological processes through phosphorylation of proteins, lipids, and carbohydrates. More than 500 different types of kinases have been identified in the human genome, which are classified based on their structure, substrate specificity, and the location of phosphorylated residues on the substrate.[1,2] Kinases regulate cell growth and division, cell differentiation, apoptosis, and immune response.[3] However, abnormal activation of these enzymes can contribute to the development of various diseases, such as cancer and autoimmune diseases. Kinases are important biological targets in the treatment of diseases, such as cancer and

[a]Laboratorio Síntesis Orgánica y Actividad Biológica (LSO-Act-Bio), Instituto de Química de Recursos Naturales, Universidad de Talca, Casilla 747, Talca 3460000, Chile. E-mail: mgutierrez@utalca.cl

[b]Universidad de la Amazonia, Programa de Química, Cl. 17 Diagonal 17 con, Cra. 3F, Florencia 180001, Colombia

[c]Doctorado en Química, Departamento de Química Inorgánica y Analítica, Universidad de Chile, Santiago, Chile

[d]Departamento de Química, Facultad de Ciencias Básicas, Universidad de Antofagasta, Avenida. Universidad de Antofagasta, Campus Coloso, Antofagasta 02800, Chile

[e]Departamento de Química, Facultad de Ciencias, Universidad Católica del Norte, Sede Casa Central, Av. Angamos 0610, Antofagasta, Chile

[f]Grupo de Investigación en Compuestos Heterocíclicos, Universidad del Atlántico, Puerto Colombia 081007, Colombia

[g]Instituto de Química de Recursos Naturales (IQRN), Universidad de Talca, Avenida Lircay S/N, Casilla 747, Talca, Chile

[h]Center for Bioinformatics and Integrative Biology, Facultad de Ciencias de la Vida, Universidad, Andrés Bello, Av. Republica 330, Santiago 8370146, Chile. E-mail: yorley.duarte@unab.cl

[i]Interdisciplinary Centre for Neuroscience of Valparaíso, Facultad de Ciencias, Universidad de Valparaíso, Valparaíso 2381850, Chile
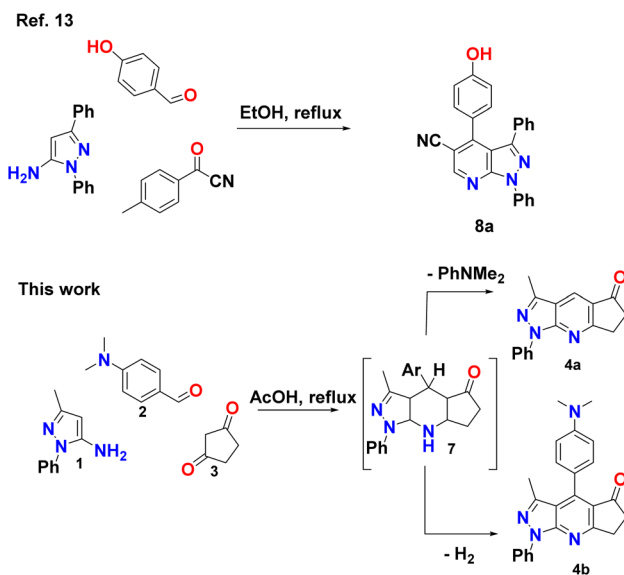
† Electronic supplementary information (ESI) available. CCDC 2278999 and 2279000. For ESI and crystallographic data in CIF or other electronic format see DOI: https://doi.org/10.1039/d3ra04874h

inflammatory diseases, and kinase inhibitors are a therapeutic option to block the activity of abnormal kinases, thereby reducing uncontrolled cell growth, destruction, and inflammation.[4]

Human protein kinases use adenosine triphosphate (ATP) for phosphorylate serine, threonine, or tyrosine residues in their target proteins. This ATP-binding site is located between the two lobes of the protein and is connected by a hinge region with a short chain of hydrogen-bonded clusters in an acceptor–donor–acceptor arrangement (see Fig. 1). Both ATP and most ATP-competing kinase inhibitors use hydrogen-bond interactions with the hinge region. Generally, kinase inhibitors are designed around a heterocyclic scaffold that forms hydrogen bonds with the hinge region and interacts with an ATP-binding pocket.[5]

Different heterocyclic structures serve as the basis for the generation of kinase inhibitors, among which pyrazolo[3,4-*b*] pyridine derivatives stand out, in addition to demonstrating interesting inhibitory properties in the many main families of kinases. It has biological properties such as antitumor, antioxidant, anti-inflammatory, antimicrobial, and therapeutic effects in autoimmune diseases.[2,6–11] Recently, Barghash *et al.*, reported the synthesis and evaluation of novel pyrazolo[3,4-*b*]pyridine derivatives as potential anticancer agents. Screening of pyrazolo[3,4-*b*]pyridine derivatives for antitumor activity revealed that several compounds exhibited potent anticancer effects. Among the tested compounds, pyrazolo[3,4-*b*]pyridine **8a** showed the most efficient antiproliferative activity, with broad-spectrum activity against almost all examined cancer cell lines (Scheme 1).[12] This study suggests that these derivatives have the potential to be used as lead molecules for the development of potent anticancer candidates.[12–15]

However, it has been reported that this heterocyclic system possesses two key structural features for kinase inhibition: (a) its ability to form hydrogen bonds and (b) its combination of pyrrolo[2,3-*b*]pyridine and an indazole moiety, which allows it to achieve multiple modes of binding both at the hinge region and at different active kinase-binding sites (see Fig. 1).[5] Likewise, it has been observed that this scaffold provides various

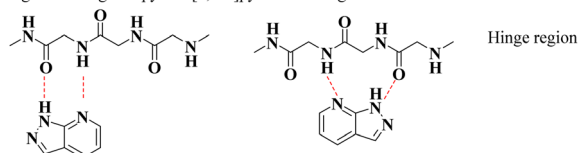**Scheme 1** Synthetic route pyrazolo[3,4-*b*]pyridine derivates.

advantages in terms of intellectual property, biological activities, physical properties, and synthetic flexibility, which has aroused great interest among researchers because of the fact that of the total number of references included in SciFinder, around pyrazolo[3,4-*b*] pyridines since 1908, more than 50% corresponds to the period from 2012 to 2022, showing an almost exponential increase, half of which are patents, clearly indicating that this type of structure currently plays an important role as a scaffold for the development of drug candidates.[15]

Computational docking is a potent method for understanding and forecasting the molecular interactions of ligands with various biological receptors such as protein active sites. This fascinating protein–ligand interaction can be used to direct the design of compounds and experiments, offering a vast pool of possibilities for therapeutic use.

The understanding of kinase–ligand interactions and selectivity has advanced significantly over the past few years. Experimentally established structures of more than 2800 catalytic kinase domains from mice and humans have shed significant light on fundamental structural factors.[16] Using this knowledge, we selected seven exemplary kinase structures for comparison. With the two most promising ligands, the emphasis was on examining the key structural characteristics in relation to their binding affinities. The structure–activity interactions of these kinases and the possible effects of our ligands were better understood through this preliminary analysis.

Taking this into account, in the present work, we synthesized and crystallized two nuclei derived from the pyrazolo[3,4-*b*] pyridine system, which were fully characterized using the experimental techniques XRD, FT-IR, HRMS, and NMR (Scheme 1). Likewise, confirmation of the stable crystal structure has been based on quantum chemistry results, such as geometry optimization, Hirshfeld surface analysis, and energy frame calculations of frontier molecular orbitals additionally, we conducted a molecular docking study of these two molecules
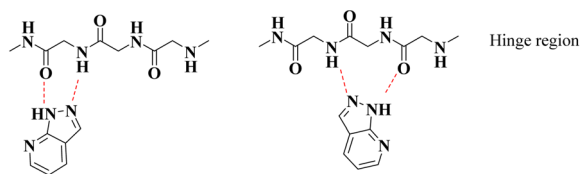

Fig. 1 Interaction of the pyrazolo[3,4-*b*]pyridine core with the hinge region of kinases. (A) Hydrogen bonding as a pyrrolo[2,3-*b*]pyridine analogue. (B) Hydrogen bonding as an indazole analogue.

against eight types of kinases linked to cancer cell lines, B-Raf proto-oncogene, serine/threonine kinase (BRAF), human epidermal growth factor receptor 2 (HER2), Colony Stimulating Factor 1 Receptor (CSF1R), Mitogen-Activated Protein Kinase 2 (MEK2), Platelet-Derived Growth Factor Receptor Alpha (PDGFRA), Janus kinase (JAK), Protein Kinase B alpha (AKT1), and Protein Kinase B beta (AKT2). This study was driven by the vast potential of pyrazolo[3,4-b]pyridine derivatives as kinase inhibitors. We were particularly interested in predicting the modes of action of the most active compounds.

2. Experimental

2.1. Materials and methods

All chemical reagents and organic solvents were obtained from commercial suppliers and were used without further purification. The experiments were performed in a Discover microwave apparatus (CEM Corporation, USA) and Branson 1510 ultrasonic cleaning bath with a mechanical timer and heater switch at 47 kHz. Thin-layer chromatography (TLC) was performed on silica gel 60 HF254 plates (Merck, Germany) to determine the purity of the compounds. The melting point ranges (m.p.) were recorded on an Electrothermal IA9100 apparatus (Stone, UK) using the one-end open capillary method and were uncorrected. IR spectra (KBr discs, 500–4000 cm^{-1}) were recorded on a NEXUS 670 FT-IR spectrophotometer (Thermo Nicolet, USA). ^{1}H and ^{13}C NMR spectra were recorded using DMSO-d_6 and CDCl$_3$ as solvents, and tetramethylsilane (TMS) as an internal reference on an AM-400 spectrometer (Bruker, Germany) at 400 and 100 MHz, respectively. High-resolution mass spectrometry (HRMS) analyses were carried out using a Bruker "Compact" quadrupole time-of-flight mass spectrometry (qTOF-MS, Germany) coupled with an Apollo II ion funnel electrospray ionization (ESI) source.

2.2. Reaction conditions to obtain pyrazolopyridine 4a and 4b

A mixture of aminopyrazole **1** (2 mmol), 4-(dimethylamino) benzaldehyde **2** (2 mmol), and cyclopentane-1,3-dione **3** (2 mmol) in glacial acetic acid (8 mL) was maintained at 120 °C for 3 h. The boiling reaction mixture was diluted with water (4 mL) and stirred. The cooled mass was filtered and the solid was washed with water. The reaction mixture was purified by column chromatography using a mixture of ethyl acetate and petroleum ether (7 : 3) to obtain compounds **4a** and **4b** Compounds **4a** and **4b** were crystallized by redissolving them in a mixture of DCM : EtOH (1 : 1), leaving them to stand until the crystals formed.

2.2.1. 3-Methyl-1-phenyl-6,7-dihydrociclopenta[2,3-e]pyrazolo[3,4-b]pyridin-5(1H)-one (4a). Yield: 40%; orange crystal, m.p. 215–217 °C; IR (KBr, cm^{-1}): 3392, 3036, 2919, 1735, 1630, 1592, 1493, 1423, 1292, 1241, 1153, 1021, 754, 664, 615, 528; ^{1}H NMR (400 MHz, DMSO-d_6): δ_H = 2.59 (s, 3H, CH$_3$), 2.76–2.80 (m, 2H), 3.22–3.25 (m, 2H) 7.35 (t, J = 7.4 Hz, 1H), 7.57 (t, J = 7.9 Hz, 2H), 8.21 (d, J = 7.8 Hz, 2H), 8.54 (s, 1H); ^{13}C NMR (100 MHz, DMSO-d_6) δ_C: 12.2 (CH$_3$), 28.5 (CH$_2$), 36.1 (CH$_2$), 116.9 (C), 120.5

(2xCH), 125.0 (C), 126.0 (CH), 127.2 (2xCH), 129.2 (CH), 138.6 (C), 145.8 (C), 152.9 (C), 174.6 (C), 203.4 (C); HRMS (ESI, m/z): calcd for C$_{16}$H$_{14}$N$_3$O [M + H]$^+$ 264.1137 found 264.1134.

2.2.2. 4-(4-(Dimethylamino)phenyl)-3-methyl-1-phenyl-6,7-dihydrocyclopenta[b]pyrazolo[4,3-e]pyridin-5(1H)-one (4b). Yield: 50%; yellow crystal, m.p. 257–259 °C; IR (KBr, cm^{-1}): 3075, 2964, 2852, 1727, 1598, 1382; ^{1}H NMR (400 MHz, (CD$_3$Cl) δ_H = 2.23 (s, 3H)), 2.77–2.80 (m, 2H), 3.06 (s, 6H), 3.28–3.32 (m, 2H), 6.81 (d, J = 8.0 Hz, 2H), 7.31–7.33 (m, 3H), 7.53 (t, J = 8.0 Hz, 2H), 8.25 (d, J = 8.0 Hz, 2H); ^{13}C NMR (100 MHz, CDCl$_3$) δ_C: 15.6 (CH$_3$), 28.3 (CH$_2$), 36.8 (CH$_2$), 40.2 (2xCH$_3$), 110.9 (2xCH), 116.0 (C), 119.4 (C), 121.5 (2xCH), 121.8 (C), 126.1 (CH), 129.0 (2xCH), 130.7 (2xCH), 139.0 (C), 145.9 (C), 147.7 (C), 150.9(C), 153.3 (C), 175.1 (C), 202.8 (C); HRMS (ESI, m/z): calcd for C$_{24}$H$_{23}$N$_4$O [M + H]$^+$ 383.1872 found 383.1867.

2.3. X-ray crystallography

Diffraction data were collected in a range of 295–296 K on a Bruker D8 Venture diffractometer equipped with a bidimensional CMOS Photon 100 detector, using graphite monochromated Mo-Kα (λ = 0.71073 Å) radiation. The diffraction frames were integrated using the APEX3 package[17] and corrected for absorption using SADABS.[18] The structure of (**1**) was solved by intrinsic phasing[19] using the OLEX2 software[20] and refined with full-matrix least-squares methods based on F^2 (SHELXL).[21] Non-hydrogen atoms were refined using anisotropic displacement parameters. The hydrogen atoms were included in their calculated positions and assigned the isotropic and shift-limited thermal parameters of their parent atoms as constants. All geometric calculations were performed using Platon software.[22]

3. Computational methods

3.1. Theoretical calculations

Density functional theory (DFT) was employed to optimize the ground-state geometries and compute the vibrational frequencies of **4a** and **4b**. These calculations were performed using the Gaussian 16 computational package with the B3LYP functional] and 6-31G* basis set.[23–28] The calculated vibrational frequencies were scaled by 0.9627.

The ionization potential (IP) and electronic affinity (EA) were estimated from the highest occupied molecular orbital (HOMO) and lowest unoccupied molecular orbital (LUMO) energies as IP = $-\varepsilon_{HOMO}$ and EA = $-\varepsilon_{LUMO}$, respectively. These estimates were employed to compute the electronegativity (χ), chemical hardness (η) and softness (S) parameters as χ = (IP + EA)/2, η = (IP − EA)/2 and S = 1/η.[29]

3.2. Hirshfeld surface analysis

CrystalExplorer 21.3 software[30] was used to calculate the Hirshfeld surface[31] and associated 2D-fingerprint plots[32] of the title compound using the crystallographic information file (CIF) as input for the analysis. The normalized contact distance d_{norm}, defined in terms of the d_e, d_i and vdW radii of the atoms, was calculated using eqn (1), where the distance from the

Hirshfeld isosurface to the nearest external (d_e) or internal (d_i) nucleus, and vdW is the van der Waals radii of atoms taken from the literature.[33,34]

$$d_{norm} = \frac{d_i + r_i^{vdw}}{r_i^{vdw}} + \frac{d_e + r_e^{vdw}}{r_e^{vdw}} \qquad (1)$$

Hirshfeld surface analysis was performed using the 6-31G(d, p) basis set at the B3LYP level of theory over a range of ± 0.002 au (ref. 35) using the TONTO computational package, which was integrated into the program CrystalExplorer.[35] The bond lengths of the hydrogen atoms involved in the interactions were normalized to standard values from neutron diffraction measurements (C–H = 1.083 Å, N–H = 1.009 Å, O–H = 0.983 Å).[36] The intermolecular energies of the molecular pairs in the crystal packing were calculated, at B3LYP/6-31G(d, p) level of theory, in a cluster of radius 3.8 Å around the molecule.[23,37]
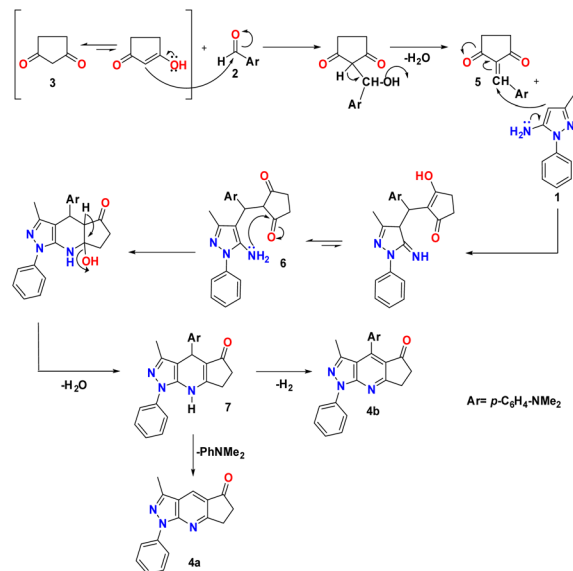
3.3. Molecular docking

Molecular docking was used to investigate the molecular basis and potential biological activity of the two pyrazolopyridine compounds as anticancer agents by targeting eight specific kinases.

The Schrödinger's Small-Molecule Drug Discovery Suite facilitated the execution of molecular docking calculations.[38] Using the Protein Preparation Wizard of Schrödinger, the basic setup of the kinase enzyme structures (BRAF – (Pdb:4MNF), HER2-(Pdb:3PP0), CSF1R-(Pdb:7MFC), MEK2 (Pdb:1S9I), PDGFRA (Pdb:6JOJ), JAK (Pdb:2B7A), AKT1 (Pdb:4GV1), and AKT2 (Pdb:2X39)) was created by adding hydrogen atoms, assigning bond ordering, generating rotamers, and protonation states. Lig-Prep software was used to construct compound structures, and ChemDraw (PerkinElmer, Waltham, Massachusetts, USA) was used to design the compound structures. Epik was used to forecast the ionization and tautomeric states. Using the impact module, the protein was subjected to molecular minimization. Furthermore, the protein was subjected to molecular minimization using the impact module. Docking calculations were carried out with Glide in the Single Precision (SP) mode, considering rigid receptors and flexible ligands. The co-crystallized ligands of the kinases served as a reference point for the grid box, and the docking grid box was oriented accordingly. Finally, Emodel was used to examine the docking poses for each molecule.

4. Results and discussion

4.1. Chemistry and characterization

A reasonable mechanism for the formation of **4a** and **4b** is presented in Scheme 2. The formation proceeds *via* initial condensation of aldehyde (**2**) with cyclopentane-1,3-dione (**3**) to give an intermediate [**5**], which further undergoes Michael addition with (**1**) to give an open-chain intermediate [**6**], which is subsequently cyclized, dehydrated and dehydrogenated to afford the aromatized intermediate [**7**] with the splitting off *N,N*-dimethylaniline and the formation of a polycondensed

Scheme 2 Plausible mechanism for the formation of pyrazolo[3,4-*b*] pyridine derivate **4a** and **4b**.

heterocyclic system with a γ-unsubstituted pyridine ring (pyrazolo[3,4-*b*]quinoline, **4a**), and in a separate process, dehydrogenated and elimination of *N,N*-dimethylaniline to afford the aromatized product **4b**.

The FT-IR spectra of the synthesized pyrazolopyridine derivatives **4a** and **4b** showed bands at the stretching frequencies of 1727–1709 cm^{-1} and 1589–1598 cm^{-1}, respectively, which are characteristic of (–C=O) and (–C=C) groups (see Table 1). ^{1}H-NMR was characterized by the presence of three groups of signals (aromatic protons, protons near heteroatoms, and aliphatic protons). In compound **4a**, a signal at approximately 8 ppm was found, which is typical of a γ-unsubstituted pyridine ring, as shown in Fig. 2.

The ^{13}C NMR spectrum of **4b** compound was measured in deuterated chloroform and revealed the presence of nineteen carbon atoms, which was consistent with the target compound (see Fig. ESI 5, 6, and Table ESI 1†). ^{13}C NMR showed a signal at δ_C = 202.8 ppm assigned to the carbonyl carbon of cyclopentanone and the signals at δ_C = 15.6 and 40.2 ppm were attributed to methyl groups, pyrazole ring and *N,N*-methyl respectively.

Electrospray ionization-mass spectrometry (ESI-MS) of compounds **4a** and **4b** exhibited $[M + H]^+$ peaks at 264.1134 and 383.1867, respectively, corresponding to the molecular formula $C_{16}H_{14}N_3O^+$ and $C_{24}H_{23}N_4O^+$ thus, based on the above spectral data, the synthesized structures were confirmed (Fig. ESI 7 and 8†).
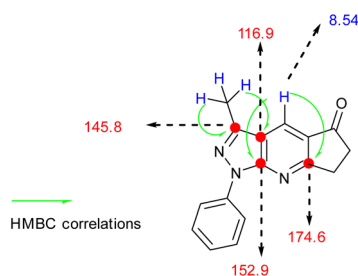
4.2. FT-IR spectra

The experimental and simulated (B3LYP/6-31G*) infrared (IR) spectra of **4a** and **4b** are shown in Fig. 3. The resulting vibrational frequencies of the optimized geometries, proposed vibrational assignments, and IR intensities are listed in Table 1. The modes are numbered from the lowest to the highest

Table 1 Comparison of calculated and experimental vibration spectra (FT-IR) of compounds **4a** and **4b**

| Normal mode | B3LYP/6-31G(d) | Experimental in this study | | Approximate |
	[a]Freq (cm^{-1})	Intensity (km mol^{-1})	Freq (cm^{-1})	assignments
4a				
1	3083	0.09	3043	Symmetric stretching C–H sp^2 (phenyl)
2	3029	0.15	3033	Asymmetric stretching C–H sp^2 (phenyl)
3	2952	0.18	2924	Symmetric stretching C–H sp^3 (N,N-dimethyl)
4	2891	0.33	2854	Asymmetric stretching C–H sp^3 (N,N-dimethyl)
5	1724	0.49	1709	Stretch C=O
6	1601	0.55	1622	Stretch C=C
7	1547	1	1589	Stretch C=C
8	1486	0.8	1495	Balanceo en el plano C–H
9	1340	0.9	1383	Stretch C–N (aryl)
4b				
1	3068	0.08	3075	Asymmetric stretching C–H sp^2 (phenyl)
2	2976	0.04	2964	Asymmetric stretching C–H sp^3 (methyl-pyrazole)
3	2929	0.07	2852	Symmetric stretching C–H sp^3 (methyl-pyrazole)
4	1739	1	1727	Stretch C=O
5	1578	0.80	1598	Stretch C=C
6	1378	0.42	1382	Out-of-plane torsion C–H

Fig. 2 Structural determination of compound **4a**.

frequency. Comparison of the theoretical and experimental IR spectra showed *t* that the strong vibrations in the experimental spectrum were also strong in the theoretical spectrum.

4.3. Frontier molecular orbitals (FMOs) analysis and molecular reactivity

As shown in Table 2, the frequencies calculated using the B3LYP/6-31G* method were in good agreement with the experimentally obtained results. Therefore, this computational method is valuable for identifying important functional groups for characterizing the molecules studied here.[39]

To obtain information on the reactivity and stability of compounds **4a** and **4b**, descriptors obtained from density
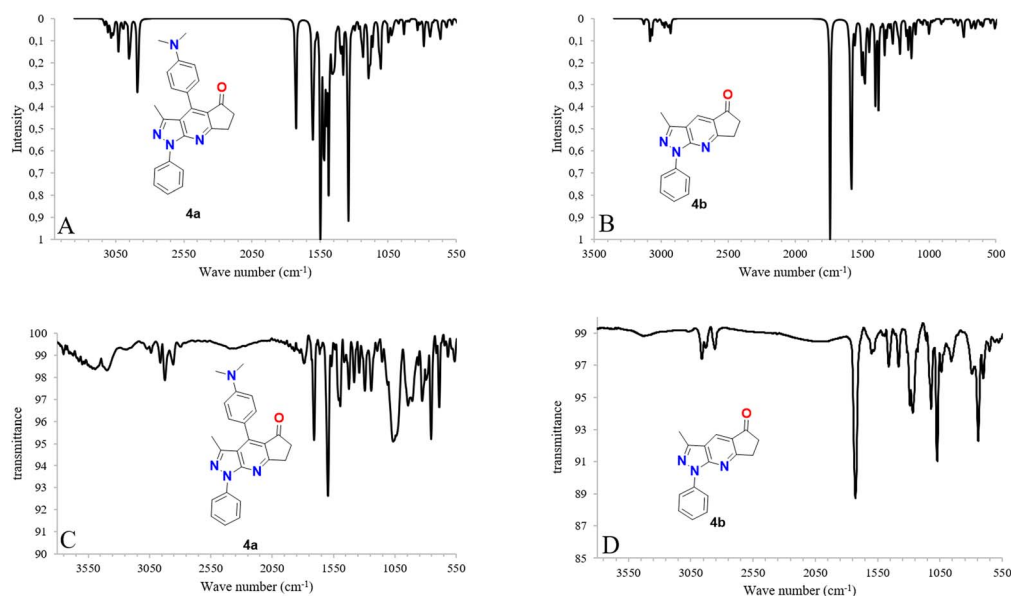

Fig. 3 IR spectra calculated with DFT (B3LYP/6-31G*) (A and B) along with experimental (C and D) IR spectra for molecules **4a** and **4b**.

Table 2 Frontier molecular orbitals energies (E_{HOMO} and E_{LUMO}), electronegativity (χ), chemical hardness (η), chemical softness (S) and electron affinity (EA)

Entry	$E_{HOMO}{}^a$	$E_{LUMO}{}^a$	ΔE^a	χ^a	η^a	S^b	EA^a
4a	−5178	−1697	3481	3438	1740	0.574	1697
4b	−5885	−1911	3975	3898	1987	0.503	1911

^{a} EV. ^{b} (EV)$^{-1}$.

functional theory were studied: HOMO and LUMO energies, HOMO–LUMO gap, hardness, softness, electronegativity, and electron affinity (see Table 2). It was found that for molecule **4a** the values were −5.178, −1.697, 3.481, 1.740, 0.574, 3.438, and 1.697 eV, respectively, while those of **4b** were −5.885, −1.911, 3.975, 1.987, 0.503, 3.898, and 1.911 eV, respectively.

The highest energy occupied molecular orbital (HOMO) characterizes the ability of a compound to donate electrons and

undergo electrophilic additions. In contrast, the energy of the lowest unoccupied molecular orbital (LUMO) supplies information about a compound's readiness to accept electrons and its susceptibility to nucleophilic attack and is related to properties such as electronegativity (tendency to attract electron density) and electron affinity (ability to accept electrons). In addition, the difference in energy between the HOMO and LUMO orbitals (HOMO–LUMO gap) provides information on chemical reactivity and kinetic stability. A molecule with a high energy gap is associated with low chemical reactivity but high kinetic stability and *vice versa* (see Fig. 4). Finally, chemical hardness and softness are related to the polarizability of a molecule. In other words, higher hardness implies lower polarizability, whereas higher softness is associated with higher polarizability.

Fig. 4 shows the molecular frontier orbitals of compounds **4a** and **4b**. For molecule **4a**, it is evident that the HOMO orbital has a high electronic density located in the 4-(dimethylamino) phenyl ring; in the case of the LUMO orbital, the region of highest probability is in the ring of the pentanone cycle; on the other hand, for the **4b** molecule, the HOMO orbital shows an electron density in the 3-methyl-1-phenylpyrazolo[3,4-*b*]pyridine nucleus, while the LUMO orbital shows that the region of highest probability lies both on the 3-methylpyrazolo[3,4-*b*] pyridine ring and on the cyclopentanone ring in the molecule.

In general, **4a** has a smaller HOMO–LUMO gap, less chemical hardness, greater chemical softness, lower electronegativity, and lower electron affinity than **4b**. Therefore, **4a** exhibits greater reactivity, less kinetic stability, greater polarizability, and less ability to attract electron density and accept electrons.
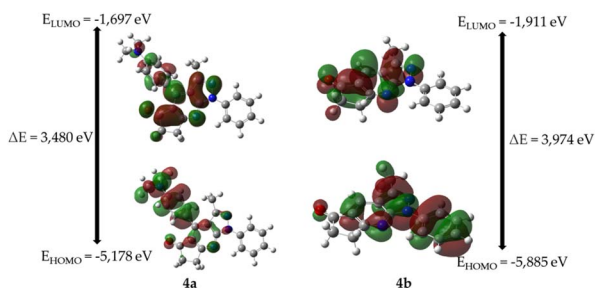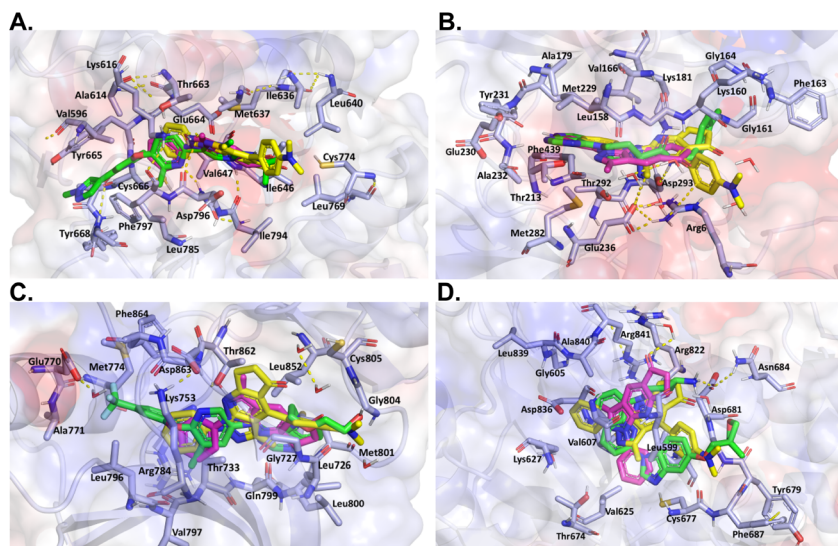

Fig. 4 Frontier molecular orbitals and related energy of compounds **4a** and **4b**.

Fig. 5 Comparative *in silico* analysis of the binding interactions between four kinases and their respective reference ligands, as well as with compounds **4a** and **4b**. In the visual representations, hydrogen bonds are depicted as yellow dashed lines, whereas hydrophobic interactions are signified by the proximity of the nearest residues, without specific visualization lines. In the figure, the reference ligands are illustrated in green, **4a** is represented in magenta, and **4b** is displayed in yellow. Panel (A) binding interactions of CSFR1 with its inhibitor and compounds **4a** and **4b** are displayed. Panel (B) AKT2's binding interactions with its inhibitor and compounds **4a** and **4b**. Panel (C) binding interactions of HER2 with its inhibitor and compounds **4a** and **4b** are displayed. Panel (D) binding interactions of PDGFRA with its inhibitor and compounds **4a** and **4b** are displayed. In all panels, each compound demonstrated a precise orientation in the protein's binding site that aligned seamlessly with the reference ligand. However, in some instances, the reference ligand is of a larger size.

4.4. Molecular docking

We used the two most promising ligands to understand crucial structural traits in connection with their binding affinities to some kinases implicated in carcinogenesis, taking into account kinase–ligand interactions and the number of kinase structures. To accomplish this, we used molecular docking, a method that simulates interactions between protein ligands. This discovery lays the groundwork for understanding the processes governing kinase–pyrazolopyridine interactions, possibly positioning these compounds as crucial structurally modifiable scaffolds for targeted cancer therapy.

The synthesized novel compounds were successfully docked within the active site of the kinase enzyme, demonstrating a favorable binding affinity with the active site amino acids based on several intermolecular interactions.

Eight kinases were used in the docking analysis, and the results showed that compounds **4a** and **4b** fit well into the binding site, stabilizing it mostly through hydrophobic interactions and hydrogen bonds. The docking score for compound **4a** was more negative than that of compound **4b** for the six kinases, suggesting superior affinity for these proteins (Table 3).

However, it should be noted that this affinity remained inferior to that exhibited by the corresponding reference compounds, as detailed in Table 3.

Compound **4a** has lower rigidity and smaller size, allowing it to fit better into each binding site, leading to increased binding

Table 3 Kinases–ligand interactions recorded during docking. The recorded interactions during kinase–ligand docking are as follows: hydro I. represents hydrophobic interactions, HB refers to hydrogen bond interactions, WM denotes water-mediated interactions, and π–π signifies π-stacking interactions. Ref. ligand refers to the ligand that co-crystallizes with each respective kinase

Kinase	Compound **4a** dock score (kcal mol^{-1})	Compound **4b** dock score (kcal mol^{-1})	Ref. ligand dock score (kcal mol^{-1})	Compound **4a** interactions	Compound **4b** interactions	Ref. ligand interactions
CSFR1	−7.60	−8.27	−11.18	Hydro. I: Met637, Cys774, Asp796, Ile646, Phe797, Val647, Leu640 HB: Glu633, Gly795	Hydro. I: Met637, Ile636, Thr663, Asp796, Ile646, Ile794, Val647 HB: Asp796	Hydro. I: Phe797, Glu664, Val596, Val647, Cys666, Tyr665 HB: Asp796, Cys666
AKT2	−6.05	−4.27	−10.42	Hydro. I: Met229, Asp293, Glu236, Met282, Gly161, Phe439, Thr213 HB: Tyr231, Arg6, Glu230	Hydro. I: Lys160, Val166, Thr292, lys181, Gly161 HB: Asp293, Glu236, Arg6, π-cation Arg6	Hydro. I: lys181, Val166, Tyr231, Gly164, Met229, Met282, Ala232, Thr292, Phe439 HB: Glu230, Ala232, Asp293
HER2	−8.81	−5.52	−10.74	Hydro. I: Met801, Leu800, Lys753, Asp863, Met801, Leu852, Thr733 HB: Asp863, Ile752	Hydro. I: Met801, Lys753, Thr862, Cys805, Gly727, Leu852 HB: Phe864, Arg849	Hydro. I: Leu796, Met774, Phe864, Gln799, Leu852 HB: Leu796, Asp863, Lys753, Met801, Cys805
PDGFRA	−6.94	−6.10	−9.37	Hydro. I: Cys677, Leu599, Ala625, Ala840,Val607, Arg841 HB: Aromatic HB Glu675	Hydro. I: Phe678, Tyr679, Leu599, Ala840, Cys677 HB: Asp681, Arg841, Cys677	Hydro. I: Tyr679, Asn684, Phe679, Leu599, Ala840, R841, K627 HB: Asp681, Cys677, salt bridge Asp681
BRAF	−7.70	−7.83	−11.0	Hydro. I: Trp531, Asp594, Gly466, Thr526 HB: Phe583 (π–π), Cys532, Ser536 (WM) Trp531(WM)	Hydro. I: Gly466, Leu514, Asp594, Ile527, Asn581, Gly593 HB: Cys532, Asp594	Hydro. I: Trp531, Ile527, Phe583, Gly466, Lys483 HB: Glu501, Cys532, Asn580 (WM)
MEK2	−6.24	−4.70	−9.60	Hydro. I: Arg193, Lys196, Leu119, Leu219, Cys211, Phe213, Lys101 HB: Ser216	Hydro. I: Met234, Arg193, Lys196, Leu119, Leu219, Cys211 HB: Lys101	Hydro. I: Lys196, Arg193, Leu119, Leu219, Met141 HB: Asp194, Lys101, Phe213 (π–π), Val131
JAK	−9.25	<3.0	−10.9	Hydro. I: Met929, Tyr931, Gly993, Leu855 HB: Glu930, Leu932, Leu983 (WM)	Hydro. I: — HB: —	Hydro. I: Met929, Tyr931, Gly993, Leu855, Arg980, Asn981, Gly935 HB: Glu930, Leu932
AKT1	−6.90	<3.0	−11.2	Hydro. I: Asp292, Lys158, Lys276, Asn279, Thr291 HB: Ala230	Hydro. I: — HB: —	Hydro. I: Asn279, Phe438, Lys279, Asp292, Ala230, Met281 HB: Ala230,Glu228, Met281, Glu234, Asn279

affinity. These characteristics are particularly beneficial for kinases with restricted binding sites, such as AKT1 and JAK, which possess smaller cavities incapable of accommodating larger molecules. Notably, compound **4a** demonstrated the highest affinity against JAK, with less than a 1.0 kcal mol^{-1} difference compared to the reference compound.

While all kinases have the same basic functions as enzymes that enable the transfer of a phosphate group from ATP to another molecule, are essential in cell signaling pathways, and may serve as targets for cancer treatment, there are noticeable distinctions in their active sites.[40] These variations control the molecules to which each kinase can bind. For instance, the binding sites of HER2 and CSF1R are predominantly negatively charged, which influences the types of molecules with which they can interact.[41]

In contrast, the active sites of the kinases BRAF, MEK2, and PDGFRA have neutral electrostatic characteristics.[42–44] JAK, AKT1, and AKT2 have positively charged binding sites, making them attractive to negatively charged ligands.[45–47] These electrostatic properties have significant implications for the affinities of compounds **4a** and **4b**. According to Table 3, compounds **4a** and **4b**, which are primarily positively charged owing to the presence of nitrogen heteroatoms, demonstrate strong affinities to the binding sites of the kinases HER2 and CSF1R, respectively. Here, the interactions primarily involved charge-positive residues.

On the other hand, despite its divergent electrostatic characteristics, compound **4a** can attach to JAK with a high degree of affinity because of its smaller size. According to the results of the molecular docking study, these pyrazole derivatives inhibited the activity of HER2, BRAF, JAK, PDGFRA, and AKT1.

Despite having lower docking score values than the reference ligand, the docked molecules had significant score values. Compound **4a** showed a better binding affinity to the aforementioned targets than the other two docked molecules. The theoretical foundation for the rational design of novel pyrazolopyridine compounds as cancer inhibitors was provided by these docking results. It also is essential to note that despite the existence of various drug-targeting kinases, these proteins continue to represent a significant class of drug targets. Thus, the development of specific drugs targeting these targets remains a challenge. This is where pyrazolopyridines come into play, serving as a fundamental fragment capable of binding to specific kinase pockets, and hence, constituting a critical scaffold for kinase drugs, as evidenced in several approved pharmaceuticals.[48] Moreover, the structural differences between the binding sites of kinases can be used to dock more suitable fragments, thereby aiding in the achievement of high selectivity for new molecules interacting with these proteins (Fig. 6).

4.5. X-ray structure

The molecular structures of the synthesized compounds **4a** and **4b** crystallized in monoclinic and triclinic unit cells with space groups $P\bar{1}$ ($Z = 2$) and $P2_1/n$ ($Z = 4$), respectively. The molecular structures of the compounds agreed with the spectroscopic characterization and the proposed structures, and both showed a centrosymmetric setting with normal bond distances and angles[36] (see Fig. ESI 9†). The dihedral angles between the mean planes of the phenyl and pyrazolo[3,4-*b*]pyridyl rings were 7.93(4) and 17.93(6)°, respectively, with the phenyl ring being more coplanar in compound **4a** than in **4b**.
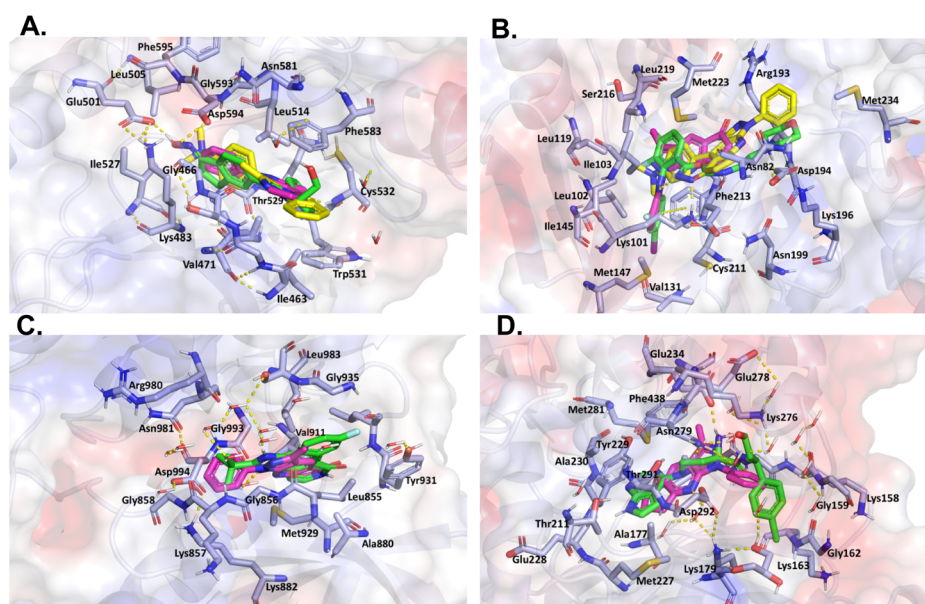

Fig. 6 Like Fig. 5, this figure presents a comparative *in silico* analysis of the binding interactions among four additional kinases and their corresponding reference ligands, as well as the interactions with compounds **4a** and **4b**. Panel (A) binding interactions of BRAF. Panel (B) binding interactions of MEK2. Panel (C) binding interactions of JAK. Panel (D) binding interactions of AKT1. In all panels, each compound demonstrates a precise orientation in the protein's binding site that aligns seamlessly with the reference ligand. However, in some instances, the reference ligand is of a larger size.

Table 4 Crystallographic data and refinement details for compound **4a** and **4b**

	4a	4b		4a	4b
Empirical formula	$C_{16}H_{13}N_3O$	$C_{24}H_{22}N_4O$	μ mm^{-1}	0.088	0.082
Formula mass (g mol^{-1})	263.29	382.45	$F(000)$	552.0	404.0
Collection T (K)	296.19	295.2	Crystal size (mm^{-3})	$0.273 \times 0.166 \times 0.145$	$0.718 \times 0.67 \times 0.504$
Crystal system	Monoclinic	Triclinic	2Θ range for data collection ($^\circ$)	5.874–52.818	7.188–61.29
Space group	$P2_1/n$	$P\bar{1}$	Index ranges (hkl)	$-10/10, -6/6, -34/34$	$-11/11, -14/14, -19/18$
a (Å)	8.7898(16)	8.0100(9)	Reflections collected	10 284	27 838
b (Å)	5.2594(9)	9.8032(11)	Independent reflections	2623	5989
				[$R_{int} = 0.0830$, $R_{sigma} = 0.0737$]	[$R_{int} = 0.0406$, $R_{sigma} = 0.0293$]
c (Å)	27.871(5)	13.6657(15)	Comp. q_{max} (%)	99.7	99.1
α ($^\circ$)	90	71.974(2)	Max/min transmission	0.735, 0.677	0.746, 0.683
β ($^\circ$)	95.483(5)	74.329(3)	Data/restraints/parameters	2623/0/199	5989/0/282
γ ($^\circ$)	90	89.987(3)	Goodness-of-fit on F^2	1.032	1.060
V (Å^3)	1282.6(4)	978.40(19)	Final R indexes [I $\geq 2\sigma$ (I)]	$R_1 = 0.0523$, w$R_2 = 0.1289$	$R_1 = 0.0595$, w$R_2 = 0.1349$
Z	4	2	Final R indexes [all data]	$R_1 = 0.0767$, w$R_2 = 0.1425$	$R_1 = 0.1031$, w$R_2 = 0.1733$
ρcalcd (g cm^{-3})	1.364	1.298	Largest diff. peak/hole/e Å^{-3}	0.23/$-$0.15	0.30/$-$0.24

In contrast, in the case of **4b**, the dihedral angle between the pyrazolo[3,4-b]pyridyl and diethylaminophenyl rings was 65.47(6)$^\circ$. A summary of the details of the crystal data and collection is presented in Table 4, and additional crystallographic details are provided in the CIF file. ORTEP views were drawn using OLEX2 software.[20]

Additionally, the crystal packing of **4a** and **4b** does not present geometrical parameters corresponding to classical hydrogen bonding[49] and is stabilized by intra- and intermolecular non-conventional hydrogen bond-like interactions C–H⋯N and C–H⋯O. In **4a**, the intramolecular C_{12}–H_{12}⋯N_1 hydrogen bond can be described using the graph set motifs S(6). Likewise, intermolecular hydrogen bond interactions generate a ring motif that can be described with R_2^2 (10) graph set motifs ($1-x$, $2-y$, $1-z$).[50] In compound **4b**, C_{14}–H_{14}⋯O1 and C_3–H_3B⋯N_3 interactions ($+x$, $1+y$, $+z$) form extended chains running along the [111] direction, forming C_1^1 (n) (n = 8 and 11) graph set motif (Fig. ESI 10†).

compound **4b**. This last feature can be attributed to the force of these interactions, with $d_i + d_e \approx 2.2$ (Fig. ESI 12†).

In addition, another type of weak interaction was observed in Hirshfeld surface analysis. For example, the ditetrel bond was verified for compound **4a** (see Fig. ESI 13†). Only a few examples of this type of interaction, which works as an electron donor in a σ-hole noncovalent bond,[51,52] with a contribution of around 5.1% with $d_e + d_i$ of > 3.6 Å, are shown as an arrow tip pattern in the fingerprint plot.

In the case of compound **4b**, π⋯π stacking was also observed, which was verified over the heterocycles in the title compound (see Fig. ESI 14†), with a contribution of approximately 1.3% with $d_e + d_i \approx 3.5$ Å. This was verified using the shape index surface, which allowed us to determine the presence of these weak interactions. The yellow–orange spots show surface subsidence owing to the proximity of the neighboring moieties, and the blue–green spots show the reciprocal contacts of the moieties that generate the subsidence.

4.6. Hirshfeld surface analysis and 2D fingerprint plots

To see other intermolecular contacts across the crystal structure, Hirshfeld surface analysis was performed to complement XRD analysis. Intermolecular interactions are constituted by C–H⋯O and, to a lesser extent, by C–H⋯N contacts, which are shown as red (d_{norm} < vdW radii), white (d_{norm} = vdW radii), and blue (d_{norm} > vdW radii) spots on the d_{norm} surfaces for all compounds. Moreover, there is evidence of another interesting weak contact in the crystal structures of all compounds. The reciprocal contacts, their respective contributions, and all fingerprint plots with d_{norm} (where $d_{norm} = d_i + d_e$) surfaces for their intermolecular contacts are shown in Fig. ESI 11.†

Additionally, the H⋯H contacts in each compound, generate a significant effect on the molecular packing in the crystal structure stabilization because their contacts are $d_i + d_e$ < 2.4 Å, in other words, these contacts are slightly shorter than the sum of the vdW radii for these atoms,[33] which can support the crystal packing of each compound as dihydrogen bond interactions. These are shown as sharp needles in **4a** and diffuse spots in

4.7. Energy frameworks

Finally, the energy framework[53] was analyzed to better understand the packing and topology of the crystal structure and supramolecular rearrangement. This method allows the calculation and comparison of different energy components, that is, repulsion (E_rep), electrostatic (E_ele), dispersion (E_dis), polarization (E_pol), and total (E_tot) energies, based on the anisotropy of the topology of pairwise intermolecular interaction energies (see Fig. ESI 15† and Table 5). The thickness of the cylinder radius indicates the grade of interactions, is directly related to the energy magnitude, and offers information about the stabilization of the crystal packing.[54] Depending on the direction of the pipe, it can be concluded that the framing is driven by translation or centrosymmetric elements. However, this rearrangement leads to the formation of another weak interaction in the crystal structure.

The results of the calculations revealed that dispersion interactions exhibit approximately honeycomb-shaped energy topologies in compound **4a**, whereas in compound **4b**, this topology zig-zag a ladder-shaped topology.

Table 5 Total energy force diagrams and the details of interaction with symmetry operation (Symop) and distances between molecular centroids (R) in Å for compounds

N	Symop	R	E_ele	E_pol	E_dis	E_rep	E_tot
4a							
1	$-x, -y, -z$	7.64	−8.7	−1.1	−44.6	25.8	−33.0
2	x, y, z	9.80	−7.0	−2.1	−14.9	9.4	−16.1
1	$-x, -y, -z$	8.24	−5.1	−1.8	−46.8	28.1	−30.1
4b							
0	$-x, -y, -z$	7.22	1.0	−1.9	−28.7	14.5	−16.4
0	$-x + 1/2, y + 1/2, -z + 1/2$	9.14	−3.3	−0.6	−15.5	10.4	−11.4
0	$x + 1/2, -y + 1/2, -z + 1/2$	15.05	0.0	−0.0	−0.1	0.0	−0.1
0	$-x + 1/2, y + 1/2, -z + 1/2$	8.01	−4.8	−0.4	−15.7	10.2	−12.7
0	$x + 1/2, -y + 1/2, z + 1/2$	14.25	−0.1	−0.0	−0.2	0.0	−0.3

5. Conclusions

Compounds **4a** and **4b** were characterized by FT-IR, HRMS, ^{1}H NMR, ^{13}C NMR, and X-ray crystallography. The X-ray findings showed that **4a** crystallized in a monoclinic system with a $P21/n$ space group, $Z = 4$, and unit cell parameters $a = 8.7898(16)$ Å, $b = 5.2594(9)$ Å, $c = 27.871(5)$ Å, $\beta = 95.483(5)°$, and $V = 1282.6(4)$ Å^3, whereas compound **4b** crystallized in the triclinic system with a $P\bar{1}$ space group, $Z = 2$, and unit cell parameters $a = 8.0100(9)$ Å, $b = 9.8032(11)$ Å, $c = 13.6657(15)$ Å, $\beta = 74.329(3)°$, and $V = 978.40(19)$ Å^3. In general, good agreement was found between all the investigated theoretical properties (structural, electronic, and spectroscopic) and the experimental results. Hirshfeld surface analysis shows that intermolecular interactions are constituted mainly by C–H⋯O contacts, and to a lesser extent by C–H⋯N contacts, for both compounds. In contrast, FMO analysis and chemical reactivity descriptors revealed that **4a** was more reactive and less stable than **4b**.

The docking results provide a theoretical basis for the rational design of novel pyrazolo[3,4-b]pyridine compounds as inhibitors for cancer treatment. This study highlighted the potential of these compounds as essential fragments capable of binding to specific kinase pockets, making them a critical scaffold for the development of kinase-targeted drugs. This observation aligns with the use of similar scaffolds in approved pharmaceutical products.

Conflicts of interest

There are no conflicts to declare.

Acknowledgements

References

1 R. Roskoski, *Pharmacol. Res.*, 2015, **100**, 1–23.

2 G. Manning, D. B. Whyte, R. Martinez, T. Hunter and S. Sudarsanam, *Science*, 2002, **298**, 1912–1934.

3 Y. Keshet and R. Seger, *Methods Mol. Biol.*, 2010, **661**, 3–38.

4 J. Zhang, P. L. Yang and N. S. Gray, *Nat. Rev. Cancer*, 2009, **9**, 28–39.

5 S. Wenglowsky, *Expert Opin. Ther. Pat.*, 2013, **23**, 281–298.

6 C. Chen, P. Pan, Z. Deng, D. Wang, Q. Wu, L. Xu, T. Hou and S. Cui, *Bioorg. Med. Chem. Lett.*, 2019, **29**, 912–916.

7 L. Jing, Y. Tang and Z. Xiao, *Bioorg. Med. Chem. Lett.*, 2018, **28**, 1386–1391.

8 A. E. M. Mekky and S. M. H. Sanad, *Polycyclic Aromat. Compd.*, 2021, **41**, 936–949.

9 S. B. Bharate, T. R. Mahajan, Y. R. Gole, M. Nambiar, T. T. Matan, A. Kulkarni-Almeida, S. Balachandran, H. Junjappa, A. Balakrishnan and R. A. Vishwakarma, *Bioorg. Med. Chem.*, 2008, **16**, 7167–7176.

10 Y. K. Abdel-Monem, S. A. Abou El-Enein and M. M. El-Sheikh-Amer, *J. Mol. Struct.*, 2017, **1127**, 386–396.

11 Y. Huang, Y. Li, G. Dong, W. Zhang, N. Liu and C. Sheng, *Arch. Pharm.*, 2018, **351**, 1–8.

12 R. F. Barghash, W. M. Eldehna, M. Kovalová, V. Vojáčková, V. Kryštof and H. A. Abdel-Aziz, *Eur. J. Med. Chem.*, 2022, **227**, 113952.

13 B. Bhukya, R. Korra and H. Guguloth, *J. Heterocycl. Chem.*, 2023, **60**, 872–878.

14 A. A. Farahat, E. M. Samir, M. Y. Zaki, R. A. T. Serya and H. A. Abdel-Aziz, *Arch. Pharm.*, 2022, **355**, 2100302.

15 A. Donaire-Arias, A. M. Montagut, R. P. de la Bellacasa, R. Estrada-Tejedor, J. Teixidó and J. I. Borrell, *Molecules*, 2022, **27**, 2237.

16 A. J. Kooistra, G. K. Kanev, O. P. J. Van Linden, R. Leurs, I. J. P. De Esch and C. De Graaf, *Nucleic Acids Res.*, 2016, **44**, D371.

17 APEX3 SAINT and SADABS Bruker, AXS Inc., Madison, Wisconsin, USA, 2015.

18 G. M. Sheldrick, *SADABS Version 2.03*, University of Göttingen, Germany, 2002.

19 G. M. Sheldrick, *Acta Crystallogr., Sect. A: Found. Adv.*, 2015, **71**, 3–8.

20 O. V Dolomanov, L. J. Bourhis, R. J. Gildea, J. A. K. Howard and H. Puschmann, *J. Appl. Crystallogr.*, 2009, **42**, 339–341.

21 G. M. Sheldrick, *Acta Crystallogr., Sect. C: Struct. Chem.*, 2015, **71**, 3–8.

22 A. L. Spek, *Acta Crystallogr., Sect. D: Biol. Crystallogr.*, 2009, **65**, 148–155.

23 A. D. Becke, *J. Chem. Phys.*, 1993, **98**, 5648–5652.

24 C. Lee, W. Yang and R. G. Parr, *Phys. Rev. B: Condens. Matter Mater. Phys.*, 1988, **37**, 785–789.

25 W. J. Hehre, K. Ditchfield and J. A. Pople, *J. Chem. Phys.*, 2003, **56**, 2257.

26 P. Geerlings, F. De Proft and W. Langenaeker, *Chem. Rev.*, 2003, **103**, 1793–1874.

27 M. J. Frisch, G. W. Trucks, H. B. Schlegel, G. E. Scuseria, M. A. Robb, J. R. Cheeseman, G. Scalmani, V. Barone, B. Mennucci, G. A. Petersson, H. Nakatsuji, M. Caricato, X. Li, H. P. Hratchian, A. V. Marenich, A. F. Izmaylov, J. Bloino, G. Zheng, J. L. Sonnenberg, M. Hada, M. Ehara, K. Toyota, R. Fukuda, J. Hasegawa, M. Ishida, T. Nakajima, Y. Honda, O. Kitao, H. Nakai, T. Vreven, J. A. Montgomery Jr., J. E. Peralta, F. Ogliaro, M. Bearpark, J. J. Heyd, E. Brothers, K. N. Kudin, V. N. Staroverov, R. Kobayashi, J. Normand, K. Raghavachari, A. Rendell, J. C. Burant, S. S. Iyengar, J. Tomasi, M. Cossi, N. Rega, J. M. Millam, M. Klene, J. E. Knox, J. B. Cross, V. Bakken, C. Adamo, J. Jaramillo, R. Gomperts, R. E. Streatmann, O. Yazyev, A. J. Austin, R. Cammi, C. Pomelli, J. W. Ochterski, R. L. Martin, K. Morokuma, V. G. Zakrzewski, G. A. Voth, P. Salvador, J. J. Danneberg, S. Dapperich, A. D. Daniels, O. Farkas, J. B. Foresman, J. V. Ortiz, J. Cioslowski and D. J. Fox, *Gaussian 09, Revision A.08*, Gaussian, Inc., Wallingford CT, 2009.

28 P. J. Stephens, F. J. Devlin, C. F. Chabalowski and M. J. Frisch, *J. Phys. Chem.*, 1994, **98**, 11623–11627.

29 F. Sonmez, Z. Gunesli, B. Z. Kurt, I. Gazioglu, D. Avci and M. Kucukislamoglu, *Mol. Diversity*, 2019, **23**, 829–844.

30 P. R. Spackman, M. J. Turner, J. J. McKinnon, S. K. Wolff, D. J. Grimwood, D. Jayatilaka and M. A. Spackman, *J. Appl. Crystallogr.*, 2021, **54**, 1006–1011.

31 M. A. Spackman and D. Jayatilaka, *CrystEngComm*, 2009, **11**, 19–32.

32 M. A. Spackman and J. J. McKinnon, *CrystEngComm*, 2002, **4**, 378–392.

33 A. Bondi, *J. Phys. Chem.*, 1964, **68**, 441–451.

34 S. S. Batsanov, *Inorg. Mater.*, 2001, **37**, 871–885.

35 M. A. Spackman, J. J. McKinnon and D. Jayatilaka, *CrystEngComm*, 2008, **10**, 377–388.

36 F. H. Allen, O. Kennard, D. G. Watson, L. Brammer, A. G. Orpen and R. Taylor, *J. Chem. Soc.*, 1987, **2**, S1–S19.

37 J. Tirado-Rives and W. L. Jorgensen, *J. Chem. Theory Comput.*, 2008, **4**, 297–306.

38 S. M. Anjum, K. S. Kumar, A. Umamaheswari, D. Lakhanpal, S. Swargam, K. Riazunnisa and T. Chandrasekhar, *Results Chem.*, 2023, **5**, 100970.

39 E. Polo-Cuadrado, C. Rojas-Peña, K. Acosta-Quiroga, L. Camargo-Ayala, I. Brito, J. Cisterna, F. Moncada, J. Trilleras, Y. A. Rodríguez-Núñez and M. Gutierrez, *RSC Adv.*, 2022, **12**, 33032–33048.

40 J. A. Adams, *Chem. Rev.*, 2001, **101**, 2271–2290.

41 Z. Hartman, W. J. Geldenhuys and Y. M. Agazie, *J. Biol. Chem.*, 2020, **295**, 3563–3575.

42 D. Nguyen, L. Y. Lin, J. O. Zhou, E. Kibby, T. W. Sia, T. D. Tillis, N. Vapuryan, M. R. Xu, R. Potluri, Y. Shin, E. A. Erler, N. Bronkema, D. J. Boehlmer, C. D. Chung, C. Burkhard, S. H. Zeng, M. Grasso, L. A. Acevedo, R. Marmorstein and D. Fera, *Biochemistry*, 2020, **59**, 4755.

43 S. Keretsu, S. Ghosh and S. J. Cho, *Int. J. Mol. Sci.*, 2020, **21**, 8232.

44 J. A. Martinez Fiesco, D. E. Durrant, D. K. Morrison and P. Zhang, *Nat. Commun.*, 2022, **13**, 1–14.

45 K. Sanachai, P. Mahalapbutr, K. Choowongkomon, R. P. Poo-Arporn, P. Wolschann and T. Rungrotmongkol, *ACS Omega*, 2020, **5**, 369–377.

46 S. Lu, R. Deng, H. Jiang, H. Song, S. Li, Q. Shen, W. Huang, R. Nussinov, J. Yu and J. Zhang, *Structure*, 2015, **23**, 1725–1734.

47 I. S. Lucet, E. Fantino, M. Styles, R. Bamert, O. Patel, S. E. Broughton, M. Walter, C. J. Burns, H. Treutlein, A. F. Wilks and J. Rossjohn, *Blood*, 2006, **107**, 176–183.

48 Z. Z. Wang, X. X. Shi, G. Y. Huang, G. F. Hao and G. F. Yang, *Trends Pharmacol. Sci.*, 2021, **42**, 551–565.

49 T. Steiner, *Angew. Chem., Int. Ed.*, 2002, **41**, 48–76.

50 J. Bernstein, R. E. Davis, L. Shimoni and N.-L. Chang, *Angew. Chem., Int. Ed.*, 1995, **34**, 1555–1573.

51 W. Dong, Q. Li and S. Scheiner, *Molecules*, 2018, **23**, 1681.

52 S. Scheiner, *Phys. Chem. Chem. Phys.*, 2020, **22**, 16606–16614.

53 C. F. Mackenzie, P. R. Spackman, D. Jayatilaka and M. A. Spackman, *IUCrJ*, 2017, **4**, 575–587.

54 H. A. Khamees, K. Chaluvaiah, N. A. El-Khatatneh, A. Swamynayaka, K. H. Chong, J. P. Dasappa and M. Madegowda, *Acta Crystallogr., Sect. E: Crystallogr. Commun.*, 2019, **75**, 1620–1626.